PHYSICAL REVIEW MATERIALS **3**, 124405 (2019)

Multiferroic properties of melanothallite Cu_2OCl_2

H. Guo,[1] L. Zhao,[1] W. Schmidt,[2] M. T. Fernández-Díaz,[3] Ch. Becker,[1] A. Melendez-Sans,[1] W. Peng,[1] M. Zbiri,[3]
P. Hansmann,[1] and A. C. Komarek[1,*]

[1] *Max-Planck-Institute for Chemical Physics of Solids, Nöthnitzer Strasse 40, Dresden D-01187, Germany*
[2] *Forschungszentrum Jülich GmbH, Jülich Centre for Neutron Science at ILL, 71 avenue des Martyrs, 38000 Grenoble, France*
[3] *Institut Laue-Langevin (ILL), 71 avenue des Martyrs, F-38042 Grenoble Cedex 9, France*

(Received 1 October 2019; published 16 December 2019)

Here we report on *P-E* hysteresis loop measurements that unravel the ferroelectric nature of melanothallite Cu_2OCl_2, a new multiferroic material with high critical temperature. Its spin structure was investigated by polarized and unpolarized neutron scattering experiments which reveal a cycloidal magnetic structure with vector chirality (magnetic polarity) that can be inverted by opposite poling of the sample with an inverted electric field. This shows that Cu_2OCl_2 is a spin-induced ferroelectric material. Finally, we show that the ferroelectric properties of Cu_2OCl_2 are driven by the inverse Dzyaloshinskii-Moriya interaction mechanism which is also able to predict the observed direction of the ferroelectric polarization properly. The origin of the noncollinear spin structure in melanothallite are competing AFM-FM exchange couplings which we estimate from a combined *ab initio* + cluster configuration interaction calculation.

DOI: 10.1103/PhysRevMaterials.3.124405

I. INTRODUCTION

Quasi-two-dimensional transition metal (TM) oxychlorides MOCl ($M =$ Sc, Ti, V, Cr, Fe) have been studied intensely because of their exciting magnetic and electronic properties as pressure-induced insulator-to-metal transitions and a crossover from a spin-Peierls transition at ambient pressure to a Peierls transition at high pressures [1–7]. For $M =$ Cu the TM oxychloride Cu_2OCl_2 is the mineral melanothallite [8,9]. Instead of crystallizing in the FeOCl structure it crystallizes in a different pyrochlore-like crystal structure with space group *Fddd* ($a \sim 7.4477$ Å, $b \sim 9.5989$ Å, $c \sim 9.6888$ Å). The Cu^{2+}-ions in Cu_2OCl_2 are square planar coordinated by two oxygen and two chlorine ions, see Fig. 1. These copper ions form a three-dimensional network of corner-sharing tetrahedra, thus building a deformed pyrochlore lattice and order antiferromagnetically below ∼70 K as observed in muon spin rotation/relaxation (μSR) experiments [10]. Very recently, the multiferroic properties of Cu_2OCl_2 were uncovered [11]. Specifically, the unusual high magnetic ordering temperature of ∼70 K renders melanothallite a very interesting material since it is associated with an unusually high critical temperature for a type-II multiferroic material [12,13]. Initially, a nuclear magnetic resonance (NMR) study claimed that Cu_2OCl_2 is a pyrochlore-like antiferromagnet with the so-called all-in-all-out spin structure [14]. Based on powder neutron diffraction measurements, an incommensurate magnetic structure was reported recently [11]. This incommensurate, noncollinear magnetic structure has been associated with spin-induced ferroelectricity in this recently discovered multiferroic material [11]. However, a very recent study claimed that Cu_2OCl_2 is antiferroelectric [15]. Moreover, also based on powder neutron diffraction data, a collinear magnetic structure was proposed within the same study [15]. Such a collinear magnetic structure would exclude the possibility of spin-induced multiferroicity in Cu_2OCl_2 which has only one kind of magnetic ion (i.e., Cu^{2+} ions).

Here we report on polarized and unpolarized single crystal neutron diffraction measurements that reveal a cycloidal magnetic structure with a magnetic polarity or vector chirality that can be inverted by opposite electric poling of the sample by inversion of the electric field. This magnetic structure is able to explain the initially observed [11] ferroelectric polarization in Cu_2OCl_2 by the inverse Dzyaloshinskii-Moriya interaction mechanism [$P \propto \mathbf{e}_{i,j} \times (\mathbf{S}_i \times \mathbf{S}_j)$] [16–18], thus proving that Cu_2OCl_2 is a type-II multiferroic with unusually high critical temperature.

II. EXPERIMENT

Cu_2OCl_2 single crystals were grown as described elsewhere [11]. The as-grown single crystals are twinned [11]. The *P-E* hysteresis loops were measured by the Virtual Ground method using a TF Analyzer 2000E from *aixACCT systems GmbH* which has advantages in measuring small capacitances. The dielectric constant was measured with an *AH2700A Andeen Hagerling* capacitance bridge. Polarized neutron diffraction measurements were performed on the IN12 spectrometer at the Institut Laue-Langevin (ILL) in Grenoble, France that was equipped with the cryopad setup for performing spherical neutron polarimetry. The flipping ratio of about 22.2 was determined from the nuclear Bragg reflections. For this measurement about 28 plate-like single crystals were coaligned with dimensions of the order of $\sim 10 \times 10 \times 1$ mm^3. This assembly was placed between two Al plates which served as the electrodes. At 100 K $> T_N$ an electric field was applied along the crystallographic

---

[*] Alexander.Komarek@cpfs.mpg.de

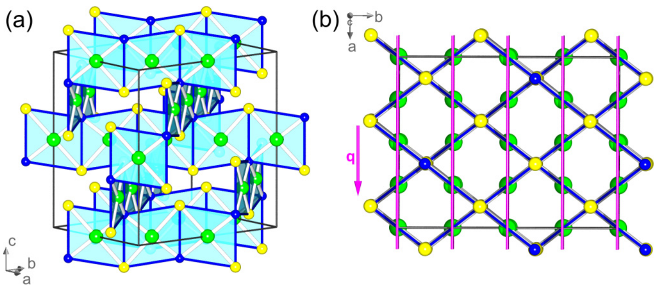

FIG. 1. Crystal structure of Cu_2OCl_2; green, blue, yellow spheres: Cu-, O-,Cl-ions, respectively. This figure visualizes the CuO_2Cl_2 plaquettes running in the [±1 1 0]-direction. The magenta arrow indicates the magnetic propagation vector **q** and the magenta planes additionally indicate the *ac*-planes through all Cu-ions which are the spiraling planes of the cycloidal spin structure of Cu_2OCl_2.

c-direction with a voltage of ±360 V followed by a cooling of the sample. After that, the neutron measurements were performed. Somehow, the voltage dropped during the cooling process and reached a value of about 170 V at 10 K. Thus, the electric field was max. 170 V/mm at the base temperature of ~2 K. Single crystal neutron diffraction measurements were performed on the D23 diffractometer at the ILL ($\lambda = 2.37$ Å). Also for these measurements about a dozen single crystals were coaligned. Complementary powder neutron diffraction data was taken from Ref. [11] ($\lambda = 2.52$ Å). In Fig. 2 the temperature dependence of a magnetic peak is shown for both powder and single crystal neutron diffraction experiments.

The way in which the polarized neutron beam is scattered is described by the Blume-Maleev equations [19,20]. For pure magnetic scattering without interference with nuclear scattering, the neutron intensities can be separated into the nonchiral terms such as $M_{\perp y}^* M_{\perp y}$, $M_{\perp z}^* M_{\perp z}$, and the chiral term $2\mathrm{Im}(M_{\perp y}^* M_{\perp z})$, where $\mathbf{M}_\perp$ is the magnetic structure factor perpendicular to the neutron momentum transfer **Q**. We use the coordinate system such that the $\widehat{x}$ direction is along **Q** direction, the $\widehat{z}$ direction is perpendicular to the scattering plane, and the $\widehat{y}$ direction is along $\widehat{z} \times \widehat{x}$. Therefore, there is no $M_{\perp x}$ component. Neglecting the incoherent scattering from the distribution of isotopes and disorder of nuclear spins, the magnetic neutron scattering intensities can be expressed as follows:

$$\begin{aligned}
I_{x\bar{x}} &\propto \mathbf{M}_\perp^* \cdot \mathbf{M}_\perp - 2\mathrm{Im}(M_{\perp y}^* M_{\perp z}),\\
I_{\bar{x}x} &\propto \mathbf{M}_\perp^* \cdot \mathbf{M}_\perp + 2\mathrm{Im}(M_{\perp y}^* M_{\perp z}),\\
I_{y\bar{x}} &\propto 1/2[\mathbf{M}_\perp^* \cdot \mathbf{M}_\perp - 2\mathrm{Im}(M_{\perp y}^* M_{\perp z})],\\
I_{yx} &\propto 1/2[\mathbf{M}_\perp^* \cdot \mathbf{M}_\perp + 2\mathrm{Im}(M_{\perp y}^* M_{\perp z})],\\
I_{z\bar{x}} &\propto 1/2[\mathbf{M}_\perp^* \cdot \mathbf{M}_\perp - 2\mathrm{Im}(M_{\perp y}^* M_{\perp z})],\\
I_{zx} &\propto 1/2[\mathbf{M}_\perp^* \cdot \mathbf{M}_\perp + 2\mathrm{Im}(M_{\perp y}^* M_{\perp z})],
\end{aligned} \tag{1}$$

where I_{ij} denotes the intensity measured with the incident neutrons polarized along the $\widehat{i}$ direction and the scattered neutrons polarized along the $\widehat{j}$ direction. Thus the chiral term can be evaluated as

$$\begin{aligned}
r_{\mathrm{chir}} &= -2\mathrm{Im}(M_{\perp y}^* M_{\perp z})/(\mathbf{M}_\perp^* \cdot \mathbf{M}_\perp)\\
&= (I_{x\bar{x}} - I_{\bar{x}x})/(I_{x\bar{x}} + I_{\bar{x}x})\\
&= (I_{y\bar{x}} - I_{yx})/(I_{y\bar{x}} + I_{yx})\\
&= (I_{z\bar{x}} - I_{zx})/(I_{z\bar{x}} + I_{zx}).
\end{aligned} \tag{2}$$

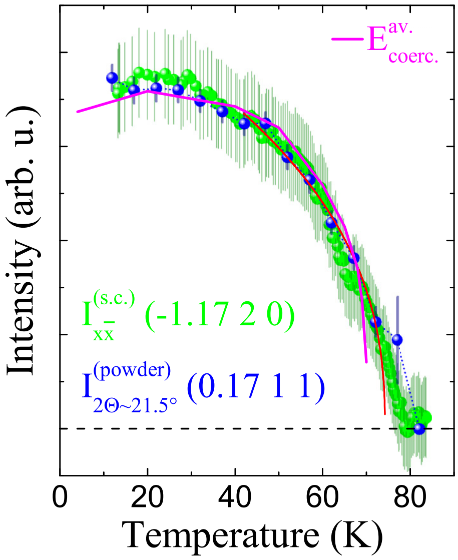

FIG. 2. Temperature dependence of the integrated intensity of the magnetic peak at $2\Theta \sim 21.5°$ in a powder neutron diffraction measurement at the D1B diffractometer (blue) and of the spin-flip intensity $I_{x\bar{x}}$ at the (−1.17 2 0) position within a single crystal neutron diffraction measurement at the IN12 spectrometer (green). Additionally, also the absolute value of the average coercive field of Cu_2OCl_2 is shown (magenta line); compare to Fig. 3.

Temperature-dependent inelastic neutron scattering measurements were performed on ~21 g of a powder of Cu_2OCl_2 using the IN4 thermal neutron time-of-flight spectrometer at the ILL. The data were collected in the down-scattering regime (neutron energy-loss mode) using two incident neutron wavelengths $\lambda_i = 1.2$ Å and $\lambda_i = 2.4$ Å. The temperature evolution of the Stokes spectrum was measured at 1.5, 60, 80, 120, 150, 200, and 300 K.

III. RESULTS

Figure 3 shows the *P*-*E* hysteresis loop measurements of Cu_2OCl_2. Clearly, the onset of the hysteretic behavior appears below the same temperature T_C where the electric polarization emerges in Cu_2OCl_2 (see the lower inset of Fig. 3) and which also coincides with the magnetic ordering temperature T_N. These results are in contrast to recent reports using a Sawyer Tower method [15] (which is usually used for larger signals) and confirms the ferroelectric nature of Cu_2OCl_2 below T_C.

The temperature dependence of the coercive field (using the average of the absolute values) is shown in Fig. 2. Well below T_N it matches roughly the temperature dependence of the magnetic peaks of the cycloidal magnetic structure. Around T_N there are substantial differences that are most likely caused by the short-ranged magnetic correlations that are already detected within neutron scattering experiments but that do not contribute to a macroscopic electric polarization. Finally, we attribute the nonsymmetrical appearance of the hysteresis

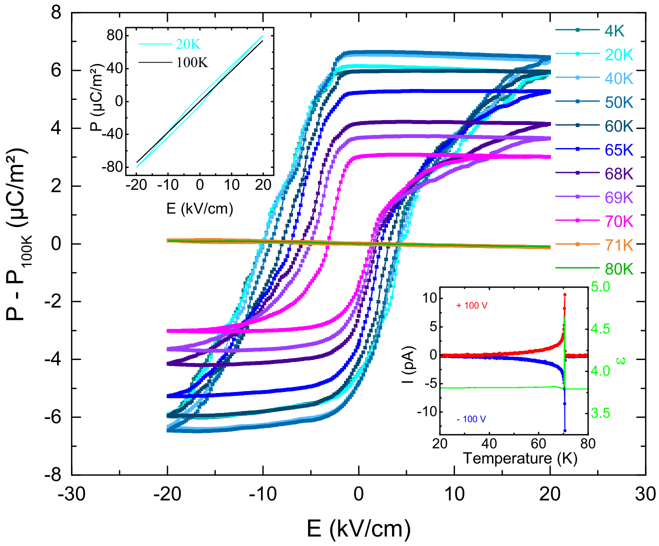

FIG. 3. *P-E* hysteresis loops of Cu_2OCl_2 measured by the Virtual Ground Method at different temperatures. Since the intrinsic signal is quite small the linear 100 K data were subtracted from *P* at lower temperatures. (The upper inset shows the raw measurement data of the *P-E* measurements at 20 and 100 K.) Below T_N a clear hysteresis can be observed which is indicative for ferroelectricity. This hysteresis vanishes between 70 and 71 K. The lower inset shows the pyroelectric current (for opposite poling) together with the dielectric constant ε that indicates the onset of the ferroelectric order which coincides with $T_N \sim 70$ K and, most importantly, with the onset temperature of the hysteretic behavior in the *P-E* curves. The coercive field is also plotted in Fig. 2 as a function of temperature.

loops in Fig. 3 to a nonequal distribution of pinning centers that influence the flipping of a cycloid into its counterpart with opposite magnetic polarity. If these pinning centers are not equally distributed for the two types of domains one could imagine that the flipping of one type of domain is somewhat hampered, which leads to different coercive fields.

Our polarized and unpolarized single crystal neutron diffraction measurements on Cu_2OCl_2 at the IN12 spectrometer and D23 diffractometer confirm the magnetic propagation vector of (∼0.83 0 0) that was derived from powder neutron diffraction measurements in Ref. [11]. In Fig. 4 neutron scattering intensities of rocking scans on the (−1.17 2 0) magnetic reflection are shown which were measured with polarized neutrons for six different channels. The experimental values of r_{chir} are listed in Table I. [e.g., for a spin spiralling within the *ac*-plane one would expect a value of $2\cos\alpha/(\cos^2\alpha + 1)$ for r_{chir}; α is the angle between $\mathbf{b}^*$ and $\mathbf{Q}$ and would amount to 37.6° for $\mathbf{Q} = (-1.17\ 2\ 0)$]. The fact that the intensities shown within each figure (e.g., $I_{x\bar{x}}$ and $I_{\bar{x}x}$) are different for the two shown channels gives nonzero values for r_{chir} in Cu_2OCl_2. Note that the electric field applied in our experiments is comparably small such that we do not expect a completed poling of the sample with one single ferroelectric domain. This might explain also the somewhat reduced values of r_{chir} in Table I.

After establishing the emergence of a noncollinear magnetic structure with vector chirality/magnetic polarity in Cu_2OCl_2, we can rule out the recently reported alternative collinear magnetic structure for Cu_2OCl_2 [15]. Furthermore, our polarized neutron experiments show that the vector chirality can be reversed by the application of an external electric field, as the relative intensity of $I_{x\bar{x}}$ and $I_{\bar{x}x}$ can be reversed by an opposite poling of the assembly of Cu_2OCl_2 single crystals. This unambiguously confirms the emergence of spin-induced ferroelectricity in Cu_2OCl_2 and rules out the antiferroelectric state claimed in Ref. [15] which is also in agreement with the observations of a macroscopic ferroelectric polarization *P* observable in pyroelectric measurements [11,15].

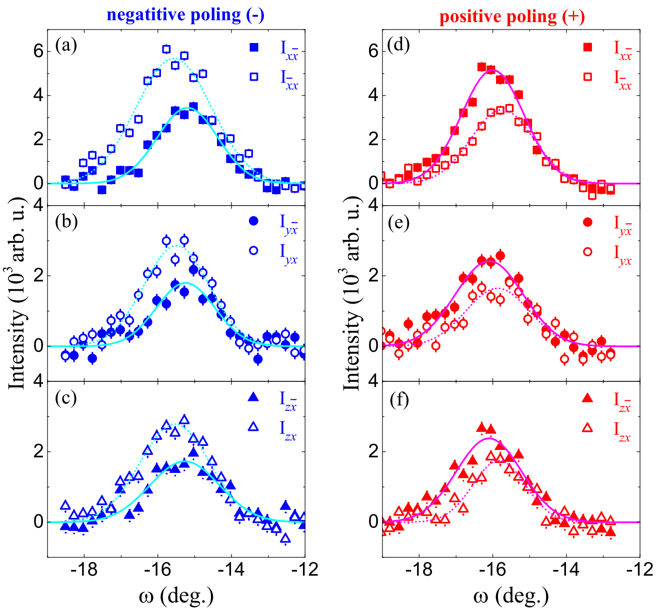

FIG. 4. Polarized neutron diffraction intensities measured at ∼2 K on the (−1.17 2 0) magnetic reflection after (a)–(c) a positive electric poling and (d)–(f) a negative electric poling. The lines are Gaussian fits to the data.

With this knowledge about the magnetic structure of Cu_2OCl_2 the microscopic mechanism that is responsible for its multiferroicity can be investigated now. In Ref. [11] no microscopic mechanism was determined due to the lack of knowledge about details of the spin structure like its (vector) chirality and just a noncollinear magnetic structure model with moments within the *ac*-plane was reported as one possible solution. Also this initially proposed noncollinear spin structure is not a spiral magnetic structure although it had been already speculated about the *"presence of a spiral magnetic structure in synthetic melanothallite"* [11]. Regarding that $r_{\mathrm{chir}} \neq 0$, which is now clearly shown by our polarized neutron scattering measurements, we reinvestigated the magnetic structure of Cu_2OCl_2 by means of single crystal

TABLE I. Experimental values of r_{chir} obtained from spherical neutron polarization analysis after a positive poling and after a negative poling.

	r_{chi}^{xx}	r_{chi}^{yx}	r_{chi}^{zx}
Positive poling	−34.8%	−27.6%	−23.4%
Negative poling	21.0%	22.1%	25.7%

TABLE II. Neutron scattering intensities I of magnetic reflections measured at the D23 diffractometer (with propagation vector $\mathbf{q} = (0.83\ 0.00\ 0.00)$; corrected for the Lorentz factor).

Reflection	Intensity I	ΔI
$(0\ 2\ 0) + \mathbf{q}$	6.60	3.12
$(0\ 2\ 0) - \mathbf{q}$	4.65	1.66
$(-2\ 0\ 2) + \mathbf{q}$	1.34	1.08
$(0\ 0\ 0) + \mathbf{q}$	5.02	0.85
$(0\ 2\ 2) + \mathbf{q}$	7.16	4.02
$(0\ 2\ 2) - \mathbf{q}$	5.75	2.08
$(0\ -2\ 0) + \mathbf{q}$	1.00	1.00
$(0\ -2\ 2) - \mathbf{q}$	1.00	1.00
$(0\ 0\ 2) + \mathbf{q}$	401.18	4.81
$(-2\ 2\ 0) + \mathbf{q}$	638.95	6.73
$(1\ 1\ 1) - \mathbf{q}$	177.44	4.47
$(-1\ 1\ 1) + \mathbf{q}$	204.21	7.30
$(1\ -1\ 1) - \mathbf{q}$	211.92	4.13
$(-1\ -1\ 1) + \mathbf{q}$	176.90	3.83
$(2\ 0\ 0) - \mathbf{q}$	5.08	2.21
$(-2\ 0\ 0) + \mathbf{q}$	1.00	0.46
$(0\ -2\ 0) - \mathbf{q}$	1.41	0.95
$(-1\ 1\ 1) - \mathbf{q}$	101.24	5.23
$(1\ -1\ 1) + \mathbf{q}$	111.00	3.51
$(1\ 0\ -1) + \mathbf{q}$	5.76	1.97
$(-1\ -1\ 1) - \mathbf{q}$	107.22	5.14
$(-1\ 1\ -1) - \mathbf{q}$	70.19	3.35

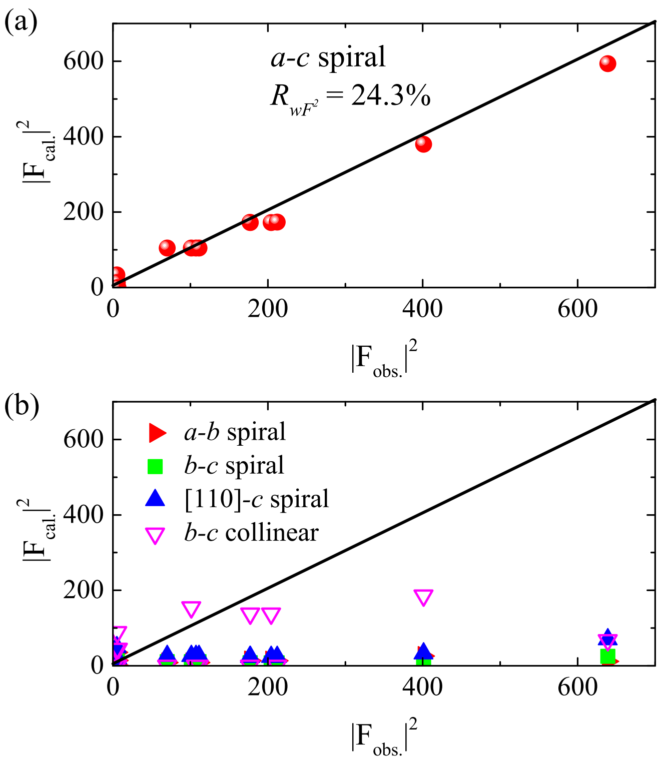

FIG. 5. Magnetic structure refinement of the single crystal neutron diffraction measurements (at 1.8 K) with (a) a circular spiral model for which the moments are constrained within the *a*-*c* plane and with (b) a circular spiral model for which the moments are constrained within the *a*-*b* plane (red triangles), the *b*-*c* plane (green squares), the [110]-*c* plane (blue triangles), and also for a collinear model (open magenta triangles) as proposed in Ref. [15].

neutron diffraction measurements that were performed at the D23 diffractometer (see Table II) and complementary powder neutron diffraction data taken from Ref. [11], see Figs. 5 and 6.

Magnetic symmetry analysis was performed using the SARAH program package [21]. With the space group *Fddd*(#70, origin 2) and propagation vector $\mathbf{k} = (0.83\ 0\ 0)$, the Cu ions at the Wyckoff position 16*d* are split into two orbits. The magnetic representation $\Gamma_{\rm mag}$ for the two orbits is decomposed into four irreducible representations of order one as follows: $\Gamma_{\rm mag} = 3\Gamma_1 + 3\Gamma_2 + 3\Gamma_3 + 3\Gamma_4$. The basis vectors for the two orbits are listed in Table III.

Having established that $r_{\rm chir} \neq 0$ (and regarding that the system is an insulator with localized moments which makes a sinusoidal modulation of the moment sizes less likely [11]) we considered four (circular) spiraling planes for each irreducible representation: (i) the *a*-*c* plane, (ii) the *a*-*b* plane, (iii) the *b*-*c* plane, and because of structural plausibility also (iv) the [110]-*c* plane in which the CuO_2Cl_2 plaquettes are running. Attempts to describe the magnetic structure with only one magnetic orbit and generation of the other magnetic moments by the *F*-centering yields no satisfactory description of the neutron data for any irreducible representation and any of the spiraling planes (see the magnetic R values in Table IV). For magnetic structure models where only two atoms from each of the two orbits were selected (with a phase factor between the two orbits that is fixed to $\phi = 2\pi k_x[x_{\#1}^{\rm orbit2}\text{-}x_{\#1}^{\rm orbit1}]$) and for generation of the other magnetic moments by the *F*-centering one, finally, obtains a good description of the experimental data for irreducible representation Γ_2 with moments spiraling within the *a*-*c* plane (see Fig. 5). This spiraling plane was already shown in Fig. 1. The magnetic structure of Cu_2OCl_2 is also shown in Fig. 7. Thus, Cu_2OCl_2 orders antiferromagnetically in a cycloidal spin structure with propagation vector in the *a*-direction and with moments spiralling within the *ac* plane, see Figs. 7(a) and 7(b). The refinement yields 0.64(5) μ_B/Cu and 0.66(2) μ_B/Cu for the ordered magnetic moment for powder and single crystal neutron refinements, respectively.

A collinear magnetic structure model with moments within the *b*-*c* plane—as proposed in Ref. [15]—has been also calculated (using the same magnetic symmetry analysis program BASIREPS as in Ref. [15]). This collinear magnetic structure model [15] cannot describe the experimental data, see Figs. 5 and 6.

Moreover, we also performed inelastic neutron scattering studies on a powder sample to probe the excitations in Cu_2OCl_2, see Fig. 8. Within the resolution of our experiments basically only phonons became apparent. To obtain further details inelastic neutron scattering experiments on large single crystals would be desirable.

The finally obtained cycloidal magnetic structure of Cu_2OCl_2 explains the observed electric polarization $\mathbf{P}$ along the *c* direction [11] according to the inverse Dzyaloshinskii-Moriya interaction mechanism in which $\mathbf{P}$ is proportional to $\mathbf{e}_{ij} \times (\mathbf{S}_i \times \mathbf{S}_j)$ with $\mathbf{e}_{ij}$ being the unit vector connecting sites i and j and with $\mathbf{S}_i$ being the moment (spin) at site i.

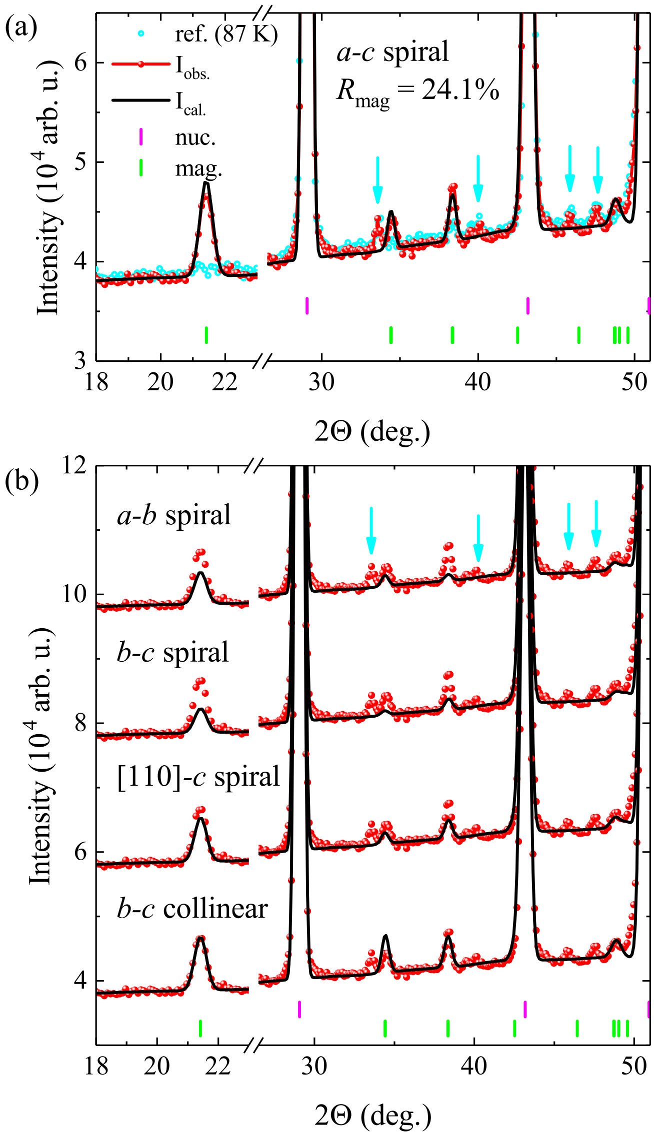

FIG. 6. Rietveld magnetic structure refinement of the powder neutron diffraction data (measured at 2 K in Ref. [11]) with a circular spiral model for which the moments are constrained (a) within the *a-c* plane, (b) within the *a-b* plane, the *b-c* plane, the [110]-*c* plane, and also for a collinear model as proposed in Ref. [15]. The 87 K data [11] in (a) is shown as a reference for the paramagnetic state. The cyan arrows indicate the peak positions originating from an impurity phase of our (hygroscopic) powder sample.

TABLE III. Nonzero IRs together with basis vectors ψ_ν for Cu ions with space group $Fddd$ (#70, origin 2) and $\mathbf{k} = (0.83\ 0\ 0)$ propagation vector obtained from representational analysis. The Cu ions at the Wyckoff 16*d* site split into two orbits with the coordinates #1: (0.5 0.5 0.5), #2: (0.5 0.25 0.25), #3: (0.75 0.5 0.75), #4: (0.75 0.75 0.5) for orbit one; and #1: (0.25 0.25 0.5), #2: (0.25 0.5 0.25), #3: (0.5 0.75 0.75), #4: (0.5 0.5 0.5) for orbit two. The phase factor φ is determined by the symmetry operation as $2\pi k_x/4$.

IRs	ψ_ν	#1	#2	#3	#4
Γ_1	ψ_1	(1, 0, 0)	(1, 0, 0)	$(-e^{i\varphi}, 0, 0)$	$(-e^{i\varphi}, 0, 0)$
	ψ_2	(0, 1, 0)	(0, −1, 0)	$(0, e^{i\varphi}, 0)$	$(0, -e^{i\varphi}, 0)$
	ψ_3	(0, 0, 1)	(0, 0, −1)	$(0, 0, -e^{i\varphi})$	$(0, 0, e^{i\varphi})$
Γ_2	ψ_1	(1, 0, 0)	(1, 0, 0)	$(e^{i\varphi}, 0, 0)$	$(e^{i\varphi}, 0, 0)$
	ψ_2	(0, 1, 0)	(0, −1, 0)	$(0, -e^{i\varphi}, 0)$	$(0, e^{i\varphi}, 0)$
	ψ_3	(0, 0, 1)	(0, 0, −1)	$(0, 0, e^{i\varphi})$	$(0, 0, -e^{i\varphi})$
Γ_3	ψ_1	(1, 0, 0)	(−1, 0, 0)	$(-e^{i\varphi}, 0, 0)$	$(e^{i\varphi}, 0, 0)$
	ψ_2	(0, 1, 0)	(0, 1, 0)	$(0, e^{i\varphi}, 0)$	$(0, e^{i\varphi}, 0)$
	ψ_3	(0, 0, 1)	(0, 0, 1)	$(0, 0, -e^{i\varphi})$	$(0, 0, -e^{i\varphi})$
Γ_4	ψ_1	(1, 0, 0)	(−1, 0, 0)	$(e^{i\varphi}, 0, 0)$	$(-e^{i\varphi}, 0, 0)$
	ψ_2	(0, 1, 0)	(0, 1, 0)	$(0, -e^{i\varphi}, 0)$	$(0, -e^{i\varphi}, 0)$
	ψ_3	(0, 0, 1)	(0, 0, 1)	$(0, 0, e^{i\varphi})$	$(0, 0, e^{i\varphi})$

For clarity, we show in Fig. 7(c) only the copper chains at $z = c/2$ and $c/4$. As can be seen, the electric polarization for the two copper chains both point along the c direction and do not cancel out. Thus the multiferroic properties of Cu_2OCl_2 originate from the emergence of a cycloidal spin structure in this compound. Our combined *ab initio* + cluster configuration interaction calculation reveal competing AFM/FM exchange couplings that are responsible for this noncollinear magnetic structure.

To show this we performed non-spin polarized (scalar relaticistic) density functional theory (DFT) calculations within the local density approximation [22] using the full potential local-orbital (FPLO) code [23]. For the Brillouin zone (BZ) integration we used the tetrahedron method with a 12 × 12 × 12 k-mesh. For the derivation of the low energy effective model we down-folded to a reduced lattice basis of Wannier functions including the full Cu 3d shell, as well as O 2p and Cl 2p. The single particle bandstructure is shown as a black solid line on the left-hand side of Fig. 9 along a selected path of high symmetry points in the Brillouin zone (the Fermi-level was set to $E_F = 0$ for this plot). Plotted in red is the single particle dispersion of the reduced Wannier basis. As is evident from this plot, the effective model agrees with the full basis

TABLE IV. Magnetic R factors obtained from Rietveld fit of the powder neutron diffraction pattern according to spiral models with moments within the *a-c*, *a-b*, *b-c*, and [110]-*c* plane. See the text for details.

	Orbit 1				Orbit 2				Orbit 1 (#1, #3) + orbit 2 (#1, #3)				orbit 1 (#1, #2) + orbit 2 (#1, #2)			
	a-c	*a-b*	*b-c*	[110]-*c*	*a-c*	*a-b*	*b-c*	[110]-*c*	*a-c*	*a-b*	*b-c*	[110]-*c*	*a-c*	*a-b*	*b-c*	[110]-*c*
Γ_1	34.4%	30.4%	41.6%	32.5%	38.3%	30.4%	36.6%	35.6%	31.0%	30.8%	58.5%	47.4%	60.9%	38.5%	33.0%	34.2%
Γ_2	52.7%	46.9%	35.6%	33.5%	54.6%	46.9%	31.4%	34.6%	**24.1%**	67.2%	78.0%	59.8%	60.9%	38.5%	33.0%	34.2%
Γ_3	52.9%	63.3%	88.5%	75.0%	54.7%	63.3%	91.6%	79.9%	31.0%	30.8%	58.5%	47.4%	77.9%	75.7%	96.2%	87.5%
Γ_4	44.2%	68.3%	85.9%	74.3%	44.2%	68.3%	88.5%	79.0%	**24.1%**	67.2%	78.0%	59.8%	77.9%	75.7%	96.2%	87.5%

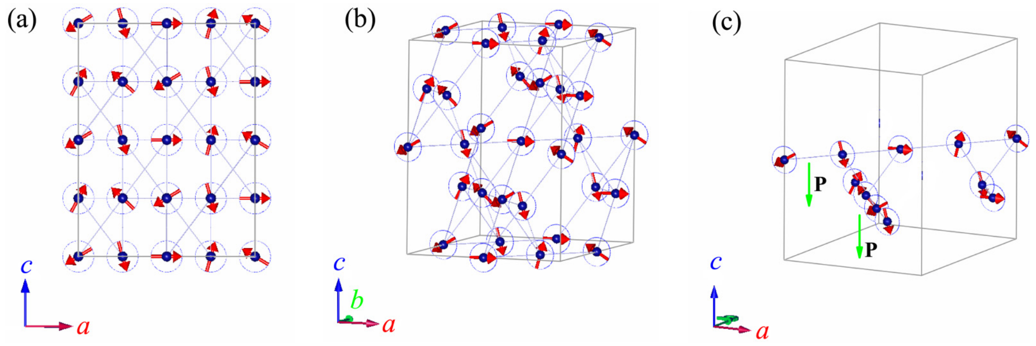

FIG. 7. (a) Magnetic structure of Cu_2OCl_2 projected along the b direction. (b) A three-dimensional view of the magnetic structure. (c) For clarity, only the copper chains running along the [1 1 0] direction at $z = c/2$ and the other ones running along the [−1 1 0] direction at $z = c/4$ are shown. The green arrows indicate the electric polarization $P \propto \mathbf{e}_{ij} \times (\mathbf{S}_i \times \mathbf{S}_j)$ for the two copper chains shown. Since P is pointing in the same direction for each copper chain, in total a macroscopic electric polarization in c-direction can be expected which is in nice agreement with experiment [11].

to a very satisfactory degree. Indeed, the good quality of the downfolding is expected as the selected low energy window [−8, +1]eV is very well separated from the rest of the Kohn-Sham spectrum.

Closer analysis of the bandstructure around the Fermi-level yields further insight (see inset in Fig. 9). Indeed the material shows four well-separated and rather narrow bands ($\approx$1 eV width) around the Fermi level each of which is at "half-filling." Analysis of the orbital character reveals a well-defined nature if considered in the proper coordinate system: The four bands originate from the antibonding linear combination of a single Cu d-orbital of a "local" $x^2 - y^2$ nature (one on each Cu site in the unit-cell) with its (symmetry-allowed) $2p$ ligands on O and Cl. The orbital analysis reveals further that the four bands are—due to conservation of orbital symmetries—very well separated from the bands in close vicinity below (<−2 eV).

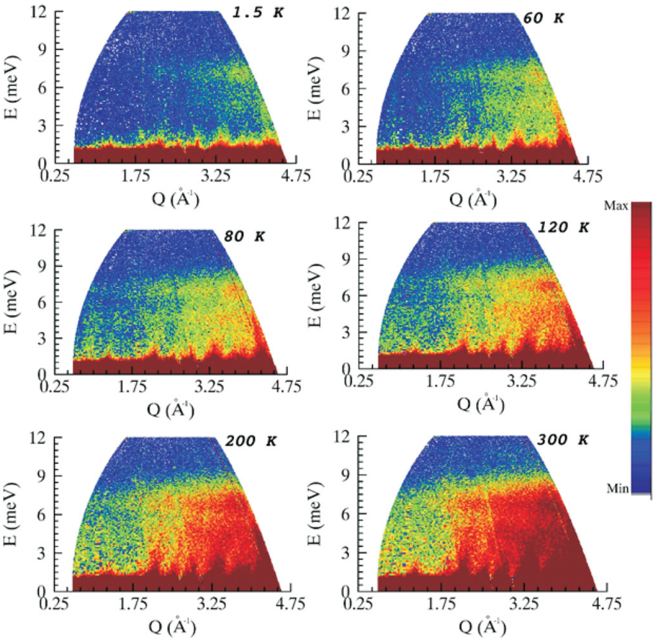

FIG. 8. The temperature evolution of the experimental Bose-factor corrected dynamical structure factor $S(\mathbf{Q},E)$ of Cu_2OCl_2 measured at the IN4 spectrometer using an incident neutron wavelength of 2.4 Å.

These unambiguous insights alone allow for important deductions without further calculations: (i) The strongly insulating character of the material is due to the effect of local interactions on the copper $3d$ orbitals. Indeed, using the generic temperature versus Hubbard U phase diagram of dynamical mean-field theory [24] we expect the Mott metal to insulator transition (for a bandwidth of 1eV) at interaction values as small as $U \approx 2.6$ eV. A direct consequence of (i) is, that Cu_2OCl_2 can be treated by means of perturbation theory around the atomic limit ($D/U \rightarrow 0$ where D is the bandwidth and U is the local Hubbard interaction). That is, we are so deep in the insulating phase that there is no need for theories like DMFT to capture renormalized Fermi liquid quasiparticles around E_F. In the following, we use such perturbative approximation to map our multiorbital model to a Heisenberg-like spin model with nonlocal exchange couplings.

A. Singlet-triplet splittings on the CI basis

A careful inspection of hopping integrals as well as the bond angles reveals that superexchange via oxygen and chlorine need to be considered carefully. On the right-hand side of Fig. 9 we show some of the relevant Wannier orbitals for the $3d$-Cu, $2p$-O, and $2p$-Cl valence state with weight around E_F (all WF plotted with identical isosurfaces). As can be seen from the plot, the relevant single $3d$-orbital per copper site can be identified as $x^2 - y^2$ in respective local coordinate systems with the z-axis perpendicular to the plane spanned by nearest neighbor O and Cl ligands.

As we did in our plot, one can distinguish two generic "directions" along which superexchagne can occur: (i) along the one-dimensional-like chains and (ii) inside the (distorted) OCu_4 tetrahedron at the intersections of the chains. At a first glance one is tempted to suspect a textbook example of ferromagnetic coupling as all Cu-O-Cu angles seem to be close to 90°. This suspicion turns out to be indeed true for the coupling along the chains, but it is wrong for some of the couplings in the tetrahedron where the angles range

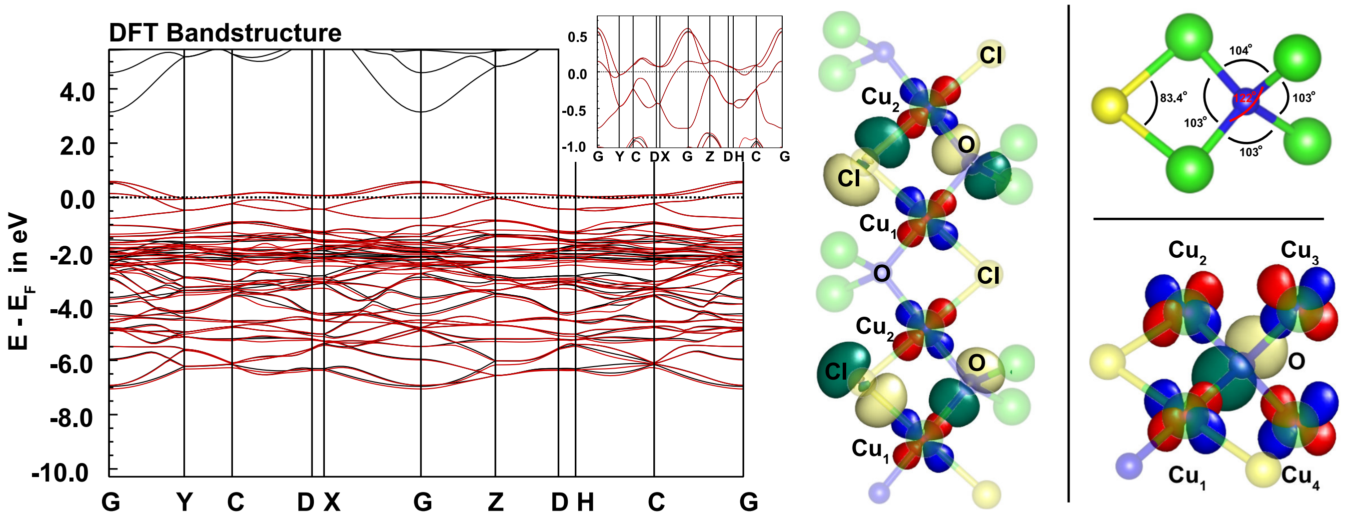

FIG. 9. Left panel: DFT bandstructure (black solid lines) along a high symmetry path in the Brillouin zone (on the energy axis 0 corresponds to the Fermi level). The bandstructure of the effective low energy (inside the a window of −8 to 1eV with respect to E_f) Wannier states are plotted in red. The inset shows a zoom around the Fermi level and highlights how well the four narrow bands around are separated from the rest. Right panels: Indication of relevant Cu-O-Cu angles and plots of selected Wannier functions contributing to the partially filled states along the CuO_2Cl_2 chains and OCu_4 tetrahedra.

from ≈102° to 122°. We remind the reader that ferromagnetic superexchange coupling originates from the combination of two conditions exactly fulfilled at a 90° bond angle: (i) the absence of a Cu-O-Cu hopping path via the same oxygen orbital and (ii) local Hund's coupling on the oxygen (or chlorine) site. At angles different from 90° Cu-O-Cu hopping paths via the same oxygen orbital are no longer symmetry forbidden and the question whether the resulting coupling is ferro or antiferromagnetic becomes a quantitative one.

The actual hopping integrals in our Wannier basis show insufficient quantitative separation of ferro and antiferromagnetic channels, such that we need to consider a larger configuration interaction basis compared to the high symmetry 90° case for the estimate of magnetic exchange paramters. To this end we take into account configurations of two copper sites at half filling (without double occupancies) as well as configurations with one or two additional electrons in the copper orbitals. The interaction parameters which define the respective configuration energy are the Hubbard U on the copper $x^2 - y^2$ orbital as well as the onsite Hund's coupling on the oxygen/chlorine site. As we intend to rationalize the origin of magnetic frustration by means of competing couplings in this correlated system we do not want to rely on ill-defined error bars for estimated interaction values. Instead we provide in Fig. 10 a parameter plot of the resulting exchange couplings as a function of Hubbard U_{Cu} on copper and the scaling of Hund's coupling around its atomic Hartree-Fock limit. In the shown contour plots the exchange coupling (as usually estimated by the singlet-triplet splitting in the CI full multiplet calculation) is coded by the color and AFM for $J_{\mathrm{ex.}} > 0$ (yellow to red) or FM for $J_{\mathrm{ex.}} < 0$ (blue colors).

Our results are unambiguous for the ferromagnetic nature of J_{12} (and by symmetry J_{34}) along the one-dimensional (1D) chains (see Fig. 10 upper right pannel): both paths—along O and Cl—seem to be close enough to the 90° high symmetry limit, such that a tiny area of AFM coupling for unrealistically small values of the interaction values is completely negligible. For the couplings inside the tetrahedron (through a single oxygen site) we find a completely different landscape (see two bottom panels of Fig. 10): For the considered interaction parameters we find a significant dependence of magnitude and,

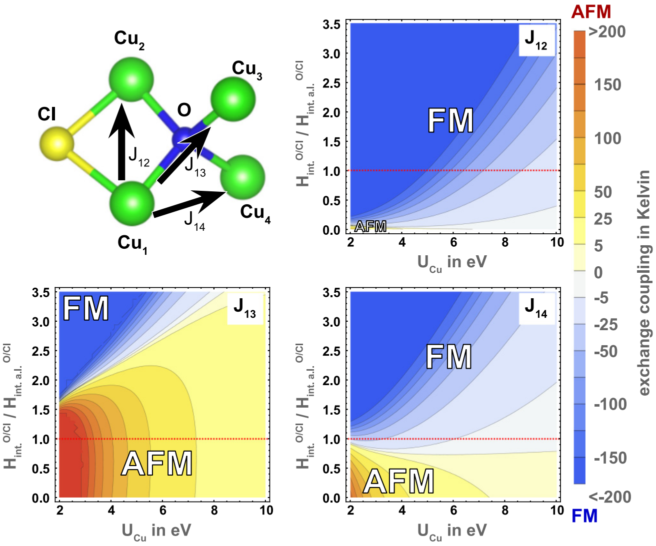

FIG. 10. Upper left: Sketch of the basic structural cluster including indications of the three different Cu-Cu superexchange couplings. Upper right and lower panels: Fals color plot of the superexchange-coupling parameter as function of onsite Hubbard U on the copper d-state and multipole Coulomb (i.e., Hund's coupling) interaction on the oxygen/chlorine sites. The red horizontal line indicates the atomic Hartree-Fock limit for the Hund's coupling.

more importantly the sign, of the exchange coupling. Indeed this dependence turns out to be crucial when considering our initial question about the ordering of the spiral magnetic order. If J_{13} and J_{14} were of identical sign, the resulting magnetic order in the ground state would be simple ferromagnetic chains coupled either ferro or antiferromagnetically to each other. However, our computation reveals that while J_{14} (along $\approx 103^\circ$) remains ferromagnetic, J_{13} (via the 122° angle) is already antiferromagnetic, which leads to frustration and likely results in the observed spiral structure.

As a final remark we add that for our conclusion the Hund's coupling on oxygen must not be screened to much below its atomic limit value. We provide two arguments that this is indeed the case: Values of interaction parameters in low energy models must never be confused for "materials constants" as they are renormalized quantities and *crucially* (by several eV) depend on the chosen energy window/Wannier basis, for which the model is formulated. Our calculations were performed on a full Cu 3*d* plus O/Cl 2*p* basis, which leads to highly localized states (which can also be seen by the contour plots of selected Wannier functions in Fig. 9). Second, screening effects considered from a more itinerant perspective for this large gap insulator are also very unlikely to significantly reduce Hund's coupling parameters.

IV. SUMMARY

Summarizing, Cu_2OCl_2 has a cycloidal spin structure with vector chirality (magnetic polarity) as observed in (polarized) neutron scattering experiments. The vector chirality/magnetic polarity can be inverted by opposite poling of the sample with an inverted electric field. This unambiguously shows that Cu_2OCl_2 is a spin-driven ferroelectric material with high critical temperature. The emergence of a cycloidal magnetic structure is able to explain the multiferroicity of melanothallite by the inverse Dzyaloshinskii-Moriya interaction mechanism including the direction of the ferroelectric polarization (*c*-direction).

ACKNOWLEDGMENTS

The research in Dresden is supported by the Deutsche Forschungsgemeinschaft through Grant No. 320571839. We thank K. Höfer for skillfull support in the *P*-*E*-loop measurements and O. Stockert for helpful discussions.

---

[1] R. Rückamp, J. Baier, M. Kriener, M. W. Haverkort, T. Lorenz, G. S. Uhrig, L. Jongen, A. Möller, G. Meyer, and M. Grüninger, Phys. Rev. Lett. **95**, 097203 (2005).

[2] A. Seidel, C. A. Marianetti, F. C. Chou, G. Ceder, and P. A. Lee, Phys. Rev. B **67**, 020405(R) (2003).

[3] V. Kataev, J. Baier, A. Möller, L. Jongen, G. Meyer, and A. Freimuth, Phys. Rev. B **68**, 140405(R) (2003).

[4] M. Shaz, S. van Smaalen, L. Palatinus, M. Hoinkis, M. Klemm, S. Horn, and R. Claessen, Phys. Rev. B **71**, 100405(R) (2005).

[5] G. Caimi, L. Degiorgi, N. N. Kovaleva, P. Lemmens, and F. C. Chou, Phys. Rev. B **69**, 125108 (2004).

[6] A. Schonleber, S. van Smaalen, and L. Palatinus, Phys. Rev. B **73**, 214410 (2006).

[7] A. C. Komarek, T. Taetz, M. T. Fernández-Díaz, D. M. Trots, A. Moller, and M. Braden, Phys. Rev. B **79**, 104425 (2009).

[8] S. V. Krivovichev, S. K. Filatov, and P. C. Burns, Can. Mineral. **40**, 1185 (2002).

[9] D. Inosov, Adv. Phys. **67**, 149 (2018).

[10] K. Kawashima, H. Okabe, K. Suzuki, S. Kuroiwa, J. Akimitsu, K. Sato, A. Koda, and R. Kadono, J. Phys.: Condens. Matter **19**, 145275 (2007).

[11] L. Zhao, M. T. Fernández-Díaz, L. H. Tjeng, and A. C. Komarek, Sci. Adv. **2**, e1600353 (2016).

[12] W. Eerenstein, N. D. Mathur, and J. F. Scott, Nature (London) **442**, 759 (2006).

[13] S.-W. Cheong and M. Mostovoy, Nat. Mater. **6**, 13 (2007).

[14] M. Nishiyama, A. Oyamada, T. Itou, S. Maegawa, H. Okabe, and J. Akimitsu, J. Phys.: Conf. Ser. **320**, 012030 (2011).

[15] H. C. Wu, J. K. Yuan, K. D. Chandrasekhar, C. H. Lee, W. H. Li, C. W. Wang, J. M. Chen, J. Y. Lin, H. Berger, T. W. Yen, S. M. Huang, C. W. Chu, and H. D. Yang, Mater. Today Phys. **8**, 34 (2019).

[16] H. Katsura, N. Nagaosa, and A. V. Balatsky, Phys. Rev. Lett. **95**, 057205 (2005).

[17] M. Mostovoy, Phys. Rev. Lett. **96**, 067601 (2006).

[18] I. A. Sergienko and E. Dagotto, Phys. Rev. B **73**, 094434 (2006).

[19] M. Blume, Phys. Rev. **130**, 1670 (1963).

[20] S. V. Maleyev, V. G. Bar'yakhtar, and R. A. Suris, Fiz. Tverd. Tela (S.-Peterburg) **4**, 3461 (1962) S. V. Maleev, V. G. Bar'yakhtar, and R. A. Suris, [Sov. Phys. Solid State **4**, 2533 (1963)].

[21] A. Wills, Physica B **276-278**, 680 (2000).

[22] J. P. Perdew and Y. Wang, Phys. Rev. B **45**, 13244 (1992).

[23] K. Koepernik and H. Eschrig, Phys. Rev. B **59**, 1743 (1999).

[24] A. Georges, G. Kotliar, W. Krauth, and J. Rozenberg, Rev. Mod. Phys. **68**, 13 (1996).